

# A new spin on LIGO-Virgo binary black holes

Sylvia Biscoveanu,<sup>1,\*</sup> Maximiliano Isi,<sup>1,†</sup> Salvatore Vitale,<sup>1</sup> and Vijay Varma<sup>2,3,‡</sup>

<sup>1</sup>LIGO Laboratory, Massachusetts Institute of Technology, Cambridge, Massachusetts 02139, USA

<sup>2</sup>TAPIR, California Institute of Technology, Pasadena, CA 91125, USA

<sup>3</sup>Department of Physics, and Cornell Center for Astrophysics and Planetary Science, Cornell University, Ithaca, New York 14853, USA

(Dated: November 28, 2021)

Gravitational waves from binary black holes have the potential to yield information on both of the intrinsic parameters that characterize the compact objects: their masses and spins. While the component masses are usually resolvable, a measurement of the component spins is generally elusive. This is partially a consequence of asking about the spins of the most and least massive objects in each binary, a question which becomes ill-defined for equal-mass systems. In this paper we show that one can ask a different question of the data: what are the spins of the most-spinning object, and of the least-spinning object, in the binary? We show that this can significantly improve estimates of the individual spins, especially for binary systems with comparable masses. When applying this parameterization to the first 13 gravitational-wave events detected by the LIGO-Virgo collaboration, we find that the most-spinning object is constrained to have nonzero spin and to have significant support at the Kerr limit for GW151226 and GW170729. A joint analysis of the first ten binary black-holes shows that the configuration where all of the spins in the population are aligned with the orbital angular momentum is excluded from the 90% credible interval, regardless of the parameterization used, reinforcing indications from previous analyses.

**Introduction.** Gravitational waves (GWs) from compact-binary coalescences (CBCs) carry imprints of the spin angular momenta  $\vec{S}$  of the black holes (BHs) or neutron stars (NSs) that originated them. The Advanced LIGO [1] and Virgo [2] detectors can extract this information to obtain key insights about the physics and astrophysics of CBCs; because the magnitude and orientation of the spins reflect the system’s history, such a measurement could potentially reveal the binary’s formation mechanism. For instance, we expect the spins of compact binaries formed in isolation to be preferentially aligned with the orbital angular momentum  $\vec{L}$  [3–12], while the same is not true of binaries formed dynamically [10, 13–17]. Identifying the formation channel of LIGO-Virgo binaries is one of the most pressing open problems in astrophysics, making the measurement of component spins a high-value target.

Unfortunately, LIGO and Virgo’s ability to measure individual component spins has, so far, been limited, since little information about these quantities is imprinted in the inspiral waveform at leading order [18–21]. At the population level, current inferences on the black hole spin distribution indicate that most sources have low spin magnitudes when considering the distributions of both the individual component spins [22, 23] and of the spin components aligned with [24–27] and perpendicular to [28] the orbital angular momentum. In this **Letter**, we show that we can draw clearer conclusions about the spins of individual objects by using a more suitable basis. Rather than attempting to identify the spin of the heaviest and lightest of the two objects, as is usually done, we infer the properties of the objects with the highest and lowest spin. This change in perspective, which amounts to a straightforward reparametrization of the problem, can

cast a new light on the component spin measurements for near-equal-mass binaries, which appear to be the majority [22, 26, 29]. In the following, we present our proposed reparametrization and demonstrate its impact both on simulated signals and on the actual LIGO-Virgo detections.

**Approach.** Within general relativity, a generic CBC signal is defined by a set of parameters encoding the intrinsic properties of the binary, as well as its spatiotemporal location. The intrinsic parameters correspond to the mass  $m_i$  and dimensionless spin  $\vec{\chi}_i = \vec{S}_i c / (Gm^2)$  of each component object  $i \in \{1, 2\}$ , plus additional quantities incorporating matter effects (e.g., tidal deformabilities for NSs) and eccentricity. Virtually all of the literature, including LIGO-Virgo collaboration papers [30–33], labels the compact objects with respect to their mass, with the index 1 corresponding to the heaviest of the two objects and 2 to the lightest, i.e.,  $m_1 \geq m_2$  by definition. However, this choice is suboptimal for systems with similar masses, as it becomes degenerate for  $m_1 = m_2$ . In that limit, the standard mass-based sorting induces undesired structure in the posteriors for the spin parameters.<sup>1</sup>

To avoid this, we instead propose to identify objects by their dimensionless spin magnitude  $\chi = |\vec{\chi}|$ , and define an equivalent set of quantities  $m_j$  and  $\vec{\chi}_j$  for  $j \in \{A, B\}$ , with  $A$  referring to the object with the highest spin and  $B$  to the lowest, i.e.  $\chi_A \geq \chi_B$  by definition. This is equivalent to a coordinate transformation effecting  $\chi_A = \max(\chi_1, \chi_2)$  and  $\chi_B = \min(\chi_1, \chi_2)$ . The mass of

<sup>1</sup> Assuming a universal equation of state, tidal parameters for binary NSs should be unaffected, since the more massive object should also be the most deformable.

the highest- $\chi$  component is  $m_A$ , just as  $\chi_1$  is the spin magnitude of the highest- $m$  component. By analogy, then, the new parametrization will impose structure in the joint  $(m_A, m_B)$  posterior when  $\chi_A = \chi_B$  (equivalently,  $\chi_1 = \chi_2$ ). However, this is not a concern if our focus is to make statements about the component spins. In the following, we will refer to the usual  $\{1, 2\}$  parametrization as *mass sorting*, and to the new  $\{A, B\}$  parameterization as *spin sorting*.

**Simulated signal.** To demonstrate the resolving power of the spin sorting, we first perform Bayesian parameter estimation on a simulated equal-mass binary black hole system with  $\chi_A = 0.8$  and  $\chi_B = 0$ . The system has a redshifted total mass of  $80 M_\odot$ , and is oriented nearly edge-on with an inclination angle  $\theta_{JN} = 80.21^\circ$ . The luminosity distance,  $d_L = 831.47$  Mpc, is chosen so that the signal is recovered with a network signal-to-noise ratio (SNR) of 30 by the two advanced LIGO instruments plus advanced Virgo, all operating at design sensitivity [1, 2]. The tilt of the spinning object is  $\theta_A = 90^\circ$  with respect to the orbital angular momentum, meaning that the spin vector lies entirely in the orbital plane.

We simulate the measurement using the `LALInference` code [34], and the numerical relativity surrogate waveform model `NRSur7dq4` [35]. We assume standard priors for LIGO-Virgo analyses [31, 34]; these imply a disjoint uniform prior on  $m_A$  and  $m_B$ , and a uniform two-dimensional prior on  $\chi_A, \chi_B$ . As is the case for  $m_1$  and  $m_2$ , the definition  $\chi_A > \chi_B$  results in a “triangular” marginal prior for  $\chi_A$  and  $\chi_B$ , i.e. a probability density linearly increasing and decreasing, respectively, with the quantity (black histograms in Fig. 1). In order to isolate the effect of the chosen parameterization on the recovered posteriors, we do not add noise to the simulated data. Further details can be found in the Appendix.

In Fig. 1, we compare the resulting measurements of the spin magnitudes and tilts using both the mass and spin sortings. The mass sorting induces a bimodal posterior in the  $\chi_1, \chi_2$  plane (symmetric around  $\chi_1 = \chi_2$ ), showing that a high spin could be assigned to either component, while the marginal posteriors on  $\chi_1$  and  $\chi_2$  are largely unconstrained. The spin sorting breaks this degeneracy, restricting the posterior so that  $\chi_A$  peaks at the true value and  $\chi_B$  rails against the lower edge of the prior. A similar degeneracy can be seen in the two-dimensional posterior for  $\theta_1$  and  $\theta_2$  in the mass sorting, which shows that information is retrieved for the tilt of one of the two objects without identifying which. Switching to the spin sorting, the  $\theta_A$  posterior is well-constrained, while  $\theta_B$  just returns the prior. Thus, this parametrization makes it clear that we can measure the tilt of the highest-spin object, but cannot say anything about the lowest-spin one. This is precisely what we would expect since  $\chi_B = 0$ , which makes  $\theta_B$  irrelevant. In Table I, we show the median recovered values and associated 90% credible interval for the component masses, spins, and tilt angles obtained

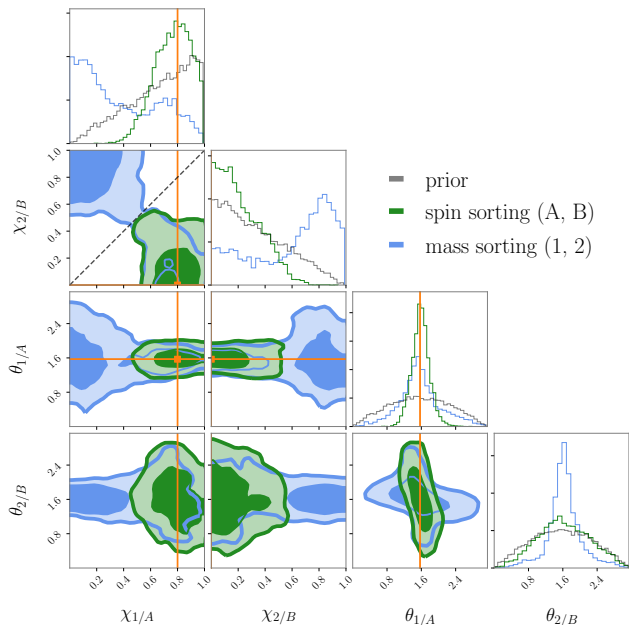


FIG. 1. Comparison corner plot showing the spin magnitudes and tilts recovered for our simulated equal-mass signal using both the mass sorting in green, and the spin sorting in blue. The marginalized one-dimensional priors for the spin sorting are shown in grey. Orange lines mark the true value, and the equal-spin diagonal is shown as a dashed line for reference.

TABLE I. Comparison of the posterior median with uncertainty quoted at the 90% level and credible interval within which the true value is recovered for the component mass and spin parameters using both the mass and spin sorting for the simulated signal.

Parameter	Inj.	Mass sorting		Spin sorting	
		Med.	CI <sub>inj</sub>	Med.	CI <sub>inj</sub>
$m_{1/A}$	$40 M_\odot$	$41.35^{+2.91}_{-1.89}$	58.5%	$39.38^{+4.14}_{-2.96}$	45.7%
$m_{2/B}$	$40 M_\odot$	$38.61^{+1.81}_{-2.63}$	67.2%	$40.49^{+2.98}_{-3.58}$	0%
$\chi_{1/A}$	0.8	$0.31^{+0.55}_{-0.29}$	87.1%	$0.77^{+0.18}_{-0.25}$	11.5%
$\chi_{2/B}$	0	$0.69^{+0.26}_{-0.64}$	61.4%	$0.19^{+0.32}_{-0.17}$	0%
$\theta_{1/A}$	1.57 rad	$1.54^{+0.97}_{-0.77}$	0%	$1.59^{+0.35}_{-0.34}$	0%
$\theta_{2/B}$	–	$1.62^{+0.72}_{-0.67}$	–	$1.60^{+1.05}_{-0.96}$	–

using both parameterizations. The statistical uncertainty for the component masses  $m_A$  and  $m_B$  is greater than for  $m_1$  and  $m_2$  because there is no imposed ordering on  $m_A$  and  $m_B$ .

In order to verify that the improved resolution of the spin sorting is robust against changes in the true spin magnitude and tilt, and that gains extend to systems without exactly equal component masses, we repeat our simulation for a variety of different binary parameters. We find a similar improvement in the resolution of the component spins for systems with lower spins,  $\chi_A = 0.2$ ,

with an aligned primary spin  $\theta_A = 0$ , and with slightly unequal mass ratios  $q = m_2/m_1 = 0.9$  when each of these parameters is varied independently in simulated signals with the same SNR as the original. When the network SNR is decreased to 12, the component spins cannot be well-measured using either parameterization.

The spin sorting ceases to be useful for systems where the mass ratio is measurably different from unity. In particular, looking at a system with  $q = 0.7$  and  $\text{SNR} = 30$ , the spin sorting introduces the same sort of degeneracies in the spin parameters as are present in Fig. 1 under the mass sorting. This is because the spin of the most massive object is well-defined for systems where the most massive object can be distinguished.

**LIGO-Virgo detections.** We apply the same reparameterization to the publicly released posterior samples for all the current LIGO-Virgo detections [30–33, 36]. The ten BBH mergers announced in the first LIGO-Virgo catalog (GWTC-1) are all consistent with  $q = 1$ , although the posteriors all support considerably lower values than the simulated signal in Fig. 1. For these systems, we find that the differences between the spin and mass sorting are generally not as significant as for the simulation; in particular, the posteriors on the tilt angles show only minimal changes between the two parameterizations.

For the two events whose posteriors in the mass sorting already indicated a preference for non-zero spins, GW151226 [37] and GW170729 [38],  $\chi_A = 0$  is ruled out with  $3\sigma$  credibility. For GW170729,  $\chi_A = \chi_B = 1$  is included within the 90% credible region, while for GW151226,  $\chi_A = 1$  is included in the 50% credible region as long as  $0.5 < \chi_B < 0.7$ . We show spin magnitude posteriors for these events using both parameterizations in Fig. 2. For the unequal-mass binary GW190412 [33], the spin sorting introduces degeneracies in the spin parameters that were not present in the mass-based sorting, which we expected from our  $q < 1$  simulations. In the Appendix, we explore the features of the GW190412 posteriors, and show that waveform systematics proved to be important for some events (including GW150914).

For the binary NSs, GW170817 [39] and GW190425 [32], two priors were used to include or exclude high spins (maximum  $\chi_i$  of 0.99 vs 0.05, respectively). For the high-spin prior, the posteriors for both  $\chi_{1/A}$  and  $\chi_{2/B}$  favor low spin values for both events and for both aligned and precessing-spin waveforms. The posteriors for the spin magnitudes are less informative for the low-spin prior, since the prior volume is considerably reduced. For GW190425, we find that the constraints on  $\cos\theta_A$  are tighter than those on  $\cos\theta_1$  for the precessing-spin waveform IMRPhenomPv2\_NRTidal,  $\cos\theta_A = 0.24^{+0.60}_{-0.44}$  compared to  $\cos\theta_1 = 0.24^{+0.62}_{-0.65}$  for the high-spin prior, and a similar trend is observed for the low-spin prior as well. Conversely, the posterior for  $\cos\theta_B$  broadens slightly compared to that of  $\cos\theta_2$ , consistent with the behavior observed for the simulated signal.

**Population analyses.** In order to determine the effects of the spin sorting on the inferred population properties of BH spins, we perform hierarchical Bayesian inference to characterize the distributions of  $\chi_A$  and  $\chi_B$ . Following [22, 40], we assume that both of the BH spins under the mass sorting are drawn from the same Beta distribution with hyper-parameters  $\alpha$  and  $\beta$  [22, 40]:

$$p(\chi_{1/2}|\alpha, \beta) = \frac{\chi_{1/2}^{\alpha-1}(1-\chi_{1/2})^{\beta-1}}{B(\alpha, \beta)}. \quad (1)$$

We further assume that the primary mass distribution is described by a truncated power-law with slope  $\alpha_m$  and upper cutoff  $m_{\text{max}}$  [41]. We fix the minimum mass to  $5 M_\odot$  and assume mass ratios to be uniformly distributed over  $(0, 1]$ . (This corresponds to Model A from [22].) We follow [22, 42] and model the distribution of spin tilts as the sum of two populations motivated by binary black hole formation channels (eg. [4, 6, 10, 43])—an isotropic component and a preferentially aligned component, where the hyper-parameters  $\sigma_{1/A}$  and  $\sigma_{2/B}$  control the spread in the possible tilt angles around  $\theta_{1/A} = \theta_{2/B} = 0$ . A nonzero value for  $\sigma$  indicates that not all tilts are aligned. The full distribution is given in the Appendix.

We apply this model to the tilt angles under both the mass and spin sorting. We use the `dynesty` sampler, as implemented in the `GWPopulation` package, to obtain hyper-parameter posterior samples [44, 45]. Our prior choices for the hyper-parameters are detailed in Table II, and further analysis details can be found in the Appendix.

If the population model for  $p(\chi_{1/2})$  is given by the Beta distribution in Eq. (1) for each of the posterior samples for the hyper-parameters  $(\alpha, \beta)$ , the population models for  $\chi_A$  and  $\chi_B$  can be determined using order statistics, assuming they correspond to the maximum and minimum of two draws from the  $\chi_{1/2}$  distribution:

$$p(\chi_A) = 2p(\chi_{1/2}|\alpha, \beta) \text{CDF}(\chi_{1/2}|\alpha, \beta), \quad (2)$$

$$p(\chi_B) = 2p(\chi_{1/2}|\alpha, \beta) [1 - \text{CDF}(\chi_{1/2}|\alpha, \beta)]. \quad (3)$$

$\text{CDF}(\chi_{1/2})$  is the cumulative distribution function for  $\chi_{1/2}$  given by the regularized incomplete Beta function with parameters  $(\alpha, \beta)$ .

In Figure 3 we show the posterior population distributions for  $p(\chi_A)$ ,  $p(\chi_B)$  and  $p(\chi_{1/2})$  as well as the 50% and 90% credible bands. The posterior population distribution is the expected distribution for the individual-event parameters of new BBH events inferred from the accumulated set of detections (see Appendix). We show results both including and excluding values of  $0 < \alpha, \beta \leq 1$ , which lead to singular configurations of the spin magnitude distributions, i.e. configurations in which  $p(\chi)$  diverges at the edges. If singular configurations are allowed, the distribution can peak at  $\chi = 0$  or  $\chi = 1$ ; if they are not, the distribution must peak within  $0 < \chi < 1$ , as nonsingular Beta distributions vanish at those values.

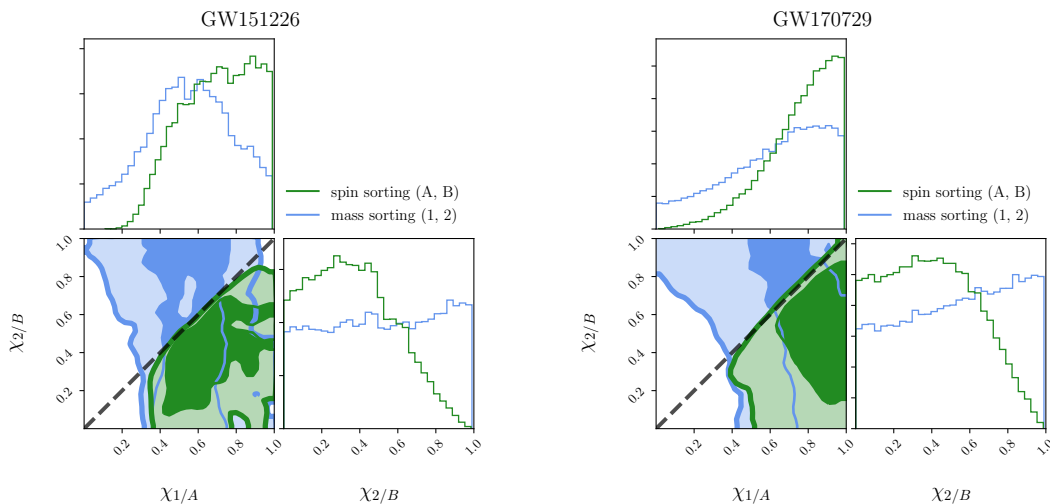


FIG. 2. Comparison corner plot for the spin magnitudes for the posteriors obtained using the IMRPhenomPv2 waveform for GW151226 and GW170729.

The inferred distribution for  $\chi_A$  indicates that most of the highest-spinning BHs in LIGO-Virgo binaries have nonzero spins, since even when singular values are allowed,  $p(\chi_A)$  has a peak at around  $\chi_A \sim 0.3$  in both configurations. The distribution of spin magnitudes for the lowest-spinning BHs is consistent with peaking at  $\chi_B = 0$ , since the distribution for  $\chi_B$  (and that for  $\chi_{1/2}$ , which agrees with the distribution inferred in [22]) only exhibits the peaked structure when singular configurations are excluded. The distributions vary significantly from those obtained using samples from the spin magnitude prior instead of posterior samples for the individual events (shown as dashed lines in Fig. 3), which are flatter for both  $p(\chi_A)$  and  $p(\chi_B)$ .

In Fig. 4, we show the posteriors on the hyperparameters describing the spin tilt population model. The blue distribution corresponds to inference starting from the mass-sorted single-event posteriors, while the green distribution shows the same for the spin-sorted posteriors (including the samples associated with singular configurations of the spin magnitude distribution being fit simultaneously). The posteriors for the mass-sorted  $\sigma_1$  and  $\sigma_2$  are consistent with those obtained in [22, 46] using a different model for the mass distribution.

The posteriors for the widths of the preferentially aligned component exhibit some variation between the two parameterizations: the posterior for  $\sigma_A$  is constrained further away from 0 than that of  $\sigma_1$ , while the opposite is true for  $\sigma_B$  and  $\sigma_2$ . The posterior for  $\sigma_B$  is consistent with having uniform support across the prior range—indicating that the information on the tilt angles at the population level is predominantly obtained from the measurement of the highest spinning object, rather than the most massive.

We highlight that  $\sigma_{1/A} = \sigma_{2/B} = 0$  is excluded with 90% credibility for both parameterizations when marginal-

ized over spin magnitude. This means that the preferentially aligned component is more likely to have nonzero width, and hence a fraction of binaries is likely to have in-plane spin components. This result agrees with previous analyses, which find that a fully-aligned population is disfavored by the LVC detections reported in GWTC-1 [22, 25, 47], and that the current detections are consistent with a population of high spins that are significantly misaligned with respect to the orbital angular momentum. [24, 27]. We confirm that this feature originates in the data—and is not just an artifact of the Monte Carlo integration—by replacing the mass-sorted spin tilt posteriors from individual events with draws from the prior. This results in an uninformative distribution for  $\sigma_1, \sigma_2$  that is consistent with having uniform support across the prior range, including the region around  $\sigma_1 = \sigma_2 = 0$  (shown in grey in Fig. 4).

**Conclusion.** We have demonstrated the advantages of introducing an alternative labeling for the component objects of a compact binary system based on their spins instead of their masses; we denote the object with the largest (smallest) spin magnitude by A (B), such that  $\chi_A > \chi_B$ . Through analysis of simulated signals, we find that this sorting improves the resolution of the component spins of binaries consistent with having equal mass, regardless of the magnitude and tilt of the primary spin. When applied to the posteriors for the GWTC-1 events, we find that the most-spinning object is consistent with having extremal spin for the events that were already known to prefer nonzero spins, GW151226 and GW170729.  $\chi_A = 0$  is ruled out at  $3\sigma$  credibility for these events. The spin sorting ceases to be useful for systems with measurably unequal masses, as was the case for GW190412.

We characterize the distributions of  $\chi_A, \chi_B, \theta_A, \theta_B$  of the GWTC-1 BBH events by means of hierarchical

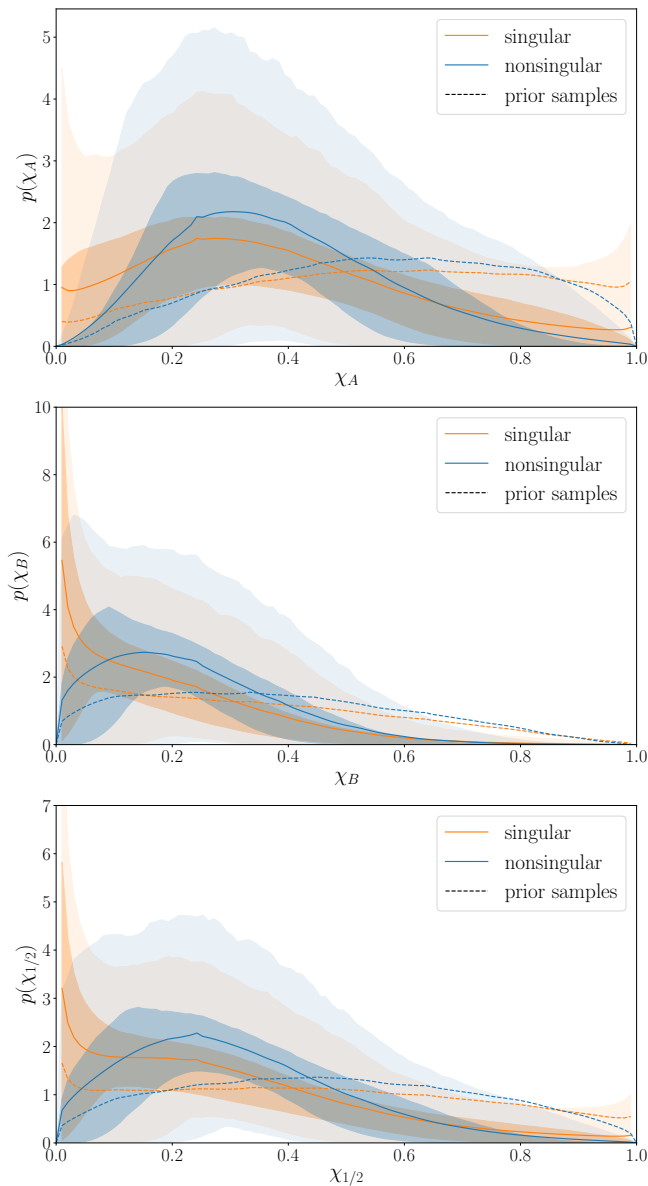


FIG. 3. Posterior population distributions for  $p(\chi_A)$  (top) and  $p(\chi_B)$  (middle) assuming they represent the maximum and minimum draws, respectively, from a distribution for the mass-sorted  $p(\chi_{1/2})$  parameterized as a beta distribution, the PPD for which is shown in the bottom panel (comparable to Fig. 8 of [22]). The blue curves include singular values for  $p(\chi)$ , while the orange curves restrict the result to nonsingular values only where  $\alpha, \beta \geq 1$ . The shaded regions correspond to the 50% and 90% credible intervals, and the PPDs obtained using prior samples for the individual events are shown in the dashed lines.

Bayesian inference. Modeling the mass-sorted spins as drawn from a Beta distribution, we compute the implied probability densities for  $\chi_A$  and  $\chi_B$  and find that  $p(\chi_A)$  peaks at  $\chi_A \sim 0.3$ , while the  $p(\chi_B)$  distribution peaks at 0. Thus, we can conclude that most of the BBHs detected by LIGO-Virgo have at least one component with

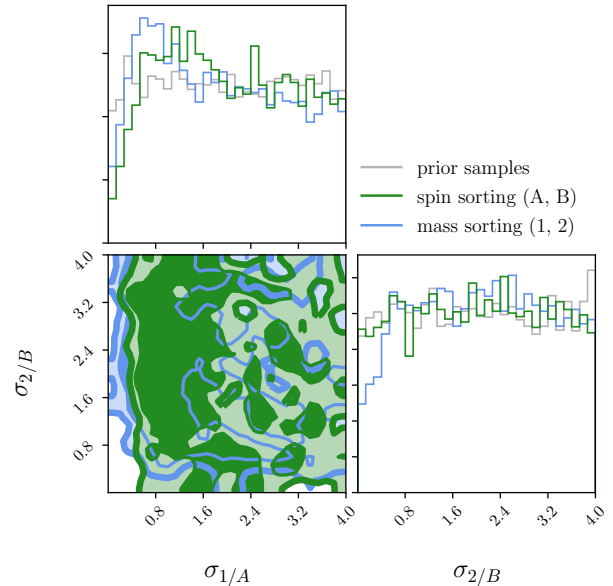


FIG. 4. Corner plot comparing the inference on the spin tilt hyper-parameters using the mass sorted tilts  $\theta_1$  and  $\theta_2$  to the posteriors obtained using the same population model but for the spin sorted tilts  $\theta_A$  and  $\theta_B$ . The posteriors obtained using prior samples for the individual events are shown in grey.

nonzero spin. When modeling the distributions of spin tilt angles, we find that the configuration where all of the spins in the population are aligned with the orbital angular momentum is excluded from the 90% credible interval, for both the mass and the spin sorting.

We end by stressing that the spin sorting does not introduce new information into the analysis: the same individual-event posterior samples are used as in the original mass-sorting, and only their labels are changed. This implies that the Bayesian evidence of the data is unchanged: the results we presented with the spin sorting are thus exactly as valid as the ones produced with the mass sorting. The reparameterization can be done entirely in post-processing and also does not change existing population-level inferences for the mass-sorted component parameters, with the possible exception of analyses relying on marginalized one-dimensional posteriors on the component spin quantities, which cannot encode the parameter degeneracies that we noted for signals consistent with  $q \approx 1$ . While in some cases the BBH formation channels make it more natural to label the component objects based on their mass, thinking about the objects in terms of spin could lead to rich new ways for testing astrophysical models moving forward.

**Acknowledgments.** S.B., M.I. and S.V. acknowledge support of the National Science Foundation and the LIGO Laboratory. LIGO was constructed by the California Institute of Technology and Massachusetts Institute of Tech-

nology with funding from the National Science Foundation and operates under cooperative agreement PHY-0757058. S.B. is also supported by the Paul and Daisy Soros Fellowship for New Americans and the NSF Graduate Research Fellowship under Grant No. DGE-1122374. M.I. is supported by NASA through the NASA Hubble Fellowship grant No. HST-HF2-51410.001-A awarded by the Space Telescope Science Institute, which is operated by the Association of Universities for Research in Astronomy, Inc., for NASA, under contract NAS5-26555. V.V. is generously supported by the Sherman Fairchild Foundation, and NSF grants PHY-170212 and PHY-1708213 at Caltech, and by a Klarman Fellowship at Cornell. The authors would like to thank Colm Talbot for help with GWPopulation, and Thomas Callister, Thomas Dent, Maya Fishbach, and Eric Thrane for careful comments on the manuscript. We also thank Will Farr, Katerina Chatziioannou, Javier Roulet, Leo Stein, Simona Miller, Carl-Johan Haster, Saavik Ford, Barry McKernan, Daniel Wysocki, Richard O’Shaughnessy, and others for useful discussions. This paper carries LIGO document number LIGO-P2000247.

---

\* sbisco@mit.edu

† NHFP Einstein fellow

‡ Klarman fellow

- [1] J. Aasi *et al.* (LIGO Scientific), *Class. Quant. Grav.* **32**, 074001 (2015), arXiv:1411.4547 [gr-qc].
- [2] F. Acernese *et al.* (VIRGO), *Class. Quant. Grav.* **32**, 024001 (2015), arXiv:1408.3978 [gr-qc].
- [3] A. V. Tutukov and L. R. YungelSon, *Monthly Notices of the Royal Astronomical Society* **260**, 675 (1993), <https://academic.oup.com/mnras/article-pdf/260/3/675/3837145/mnras260-0675.pdf>.
- [4] V. Kalogera, *Astrophys. J.* **541**, 319 (2000), arXiv:astro-ph/9911417.
- [5] P. Grandclement, M. Ihm, V. Kalogera, and K. Belczynski, *Phys. Rev. D* **69**, 102002 (2004), arXiv:gr-qc/0312084.
- [6] K. A. Postnov and L. R. Yungelson, *Living Rev. Rel.* **17**, 3 (2014), arXiv:1403.4754 [astro-ph.HE].
- [7] K. Belczynski, D. E. Holz, T. Bulik, and R. O’Shaughnessy, *Nature* **534**, 512 (2016), arXiv:1602.04531 [astro-ph.HE].
- [8] I. Mandel and S. E. de Mink, *Mon. Not. Roy. Astron. Soc.* **458**, 2634 (2016), arXiv:1601.00007 [astro-ph.HE].
- [9] Marchant, Pablo, Langer, Norbert, Podsiadlowski, Philipp, Tauris, Thomas M., and Moriya, Takashi J., *A&A* **588**, A50 (2016).
- [10] C. L. Rodriguez, M. Zevin, C. Pankow, V. Kalogera, and F. A. Rasio, *Astrophys. J. Lett.* **832**, L2 (2016), arXiv:1609.05916 [astro-ph.HE].
- [11] R. O’Shaughnessy, D. Gerosa, and D. Wysocki, *Phys. Rev. Lett.* **119**, 011101 (2017), arXiv:1704.03879 [astro-ph.HE].
- [12] S. Stevenson, A. Vigna-Gómez, I. Mandel, J. W. Barrett, C. J. Neijssel, D. Perkins, and S. E. de Mink, *Nature Commun.* **8**, 14906 (2017), arXiv:1704.01352 [astro-ph.HE].
- [13] S. Sigurdsson and L. Hernquist, *Nature* **364**, 423 (1993).
- [14] M. Miller and V. M. Lauburg, *Astrophys. J.* **692**, 917 (2009), arXiv:0804.2783 [astro-ph].
- [15] I. Mandel and R. O’Shaughnessy, *Class. Quant. Grav.* **27**, 114007 (2010), arXiv:0912.1074 [astro-ph.HE].
- [16] S. Portegies Zwart, S. McMillan, and M. Gieles, *Ann. Rev. Astron. Astrophys.* **48**, 431 (2010), arXiv:1002.1961 [astro-ph.GA].
- [17] M. J. Benacquista and J. M. Downing, *Living Rev. Rel.* **16**, 4 (2013), arXiv:1110.4423 [astro-ph.SR].
- [18] T. Damour, *Phys. Rev. D* **64**, 124013 (2001).
- [19] E. Racine, *Phys. Rev. D* **78**, 044021 (2008), arXiv:0803.1820 [gr-qc].
- [20] P. Ajith, M. Hannam, S. Husa, Y. Chen, B. Brügmann, N. Dorband, D. Müller, F. Ohme, D. Pollney, C. Reisswig, L. Santamaría, and J. Seiler, *Phys. Rev. Lett.* **106**, 241101 (2011).
- [21] K. K. Ng, S. Vitale, A. Zimmerman, K. Chatziioannou, D. Gerosa, and C.-J. Haster, *Phys. Rev. D* **98**, 083007 (2018), arXiv:1805.03046 [gr-qc].
- [22] B. Abbott *et al.* (LIGO Scientific, Virgo), *Astrophys. J. Lett.* **882**, L24 (2019), arXiv:1811.12940 [astro-ph.HE].
- [23] C. Kimball, C. Talbot, C. P. Berry, M. Carney, M. Zevin, E. Thrane, and V. Kalogera, (2020), arXiv:2005.00023 [astro-ph.HE].
- [24] W. M. Farr, S. Stevenson, M. Coleman Miller, I. Mandel, B. Farr, and A. Vecchio, *Nature* **548**, 426 (2017), arXiv:1706.01385 [astro-ph.HE].
- [25] V. Tiwari, S. Fairhurst, and M. Hannam, *Astrophys. J.* **868**, 140 (2018), arXiv:1809.01401 [gr-qc].
- [26] J. Roulet and M. Zaldarriaga, *Mon. Not. Roy. Astron. Soc.* **484**, 4216 (2019), arXiv:1806.10610 [astro-ph.HE].
- [27] S. Miller, T. A. Callister, and W. Farr, (2020), 10.3847/1538-4357/ab80c0, arXiv:2001.06051 [astro-ph.HE].
- [28] S. Fairhurst, R. Green, M. Hannam, and C. Hoy, (2019), arXiv:1908.00555 [gr-qc].
- [29] M. Fishbach and D. E. Holz, *Astrophys. J. Lett.* **891**, L27 (2020), arXiv:1905.12669 [astro-ph.HE].
- [30] R. Abbott *et al.* (LIGO Scientific, Virgo), (2019), arXiv:1912.11716 [gr-qc].
- [31] B. Abbott *et al.* (LIGO Scientific, Virgo), *Phys. Rev. X* **9**, 031040 (2019), arXiv:1811.12907 [astro-ph.HE].
- [32] B. Abbott *et al.* (LIGO Scientific, Virgo), *Astrophys. J. Lett.* **892**, L3 (2020), arXiv:2001.01761 [astro-ph.HE].
- [33] R. Abbott *et al.* (LIGO Scientific, Virgo), (2020), arXiv:2004.08342 [astro-ph.HE].
- [34] J. Veitch *et al.*, *Phys. Rev. D* **91**, 042003 (2015), arXiv:1409.7215 [gr-qc].
- [35] V. Varma, S. E. Field, M. A. Scheel, J. Blackman, D. Gerosa, L. C. Stein, L. E. Kidder, and H. P. Pfeiffer, *Phys. Rev. Research* **1**, 033015 (2019), arXiv:1905.09300 [gr-qc].
- [36] M. Vallisneri, J. Kanner, R. Williams, A. Weinstein, and B. Stephens, *J. Phys. Conf. Ser.* **610**, 012021 (2015), arXiv:1410.4839 [gr-qc].
- [37] B. P. Abbott *et al.* (LIGO Scientific, Virgo), *Phys. Rev. Lett.* **116**, 241103 (2016), arXiv:1606.04855 [gr-qc].
- [38] K. Chatziioannou *et al.*, *Phys. Rev. D* **100**, 104015 (2019), arXiv:1903.06742 [gr-qc].
- [39] B. Abbott *et al.* (LIGO Scientific, Virgo), *Phys. Rev. Lett.* **119**, 161101 (2017), arXiv:1710.05832 [gr-qc].
- [40] D. Wysocki, J. Lange, and R. O’Shaughnessy, *Phys. Rev. D* **100**, 043012 (2019).
- [41] M. Fishbach and D. E. Holz, *Astrophys. J. Lett.* **851**, L25

- (2017), arXiv:1709.08584 [astro-ph.HE].
- [42] C. Talbot and E. Thrane, *Phys. Rev. D* **96**, 023012 (2017), arXiv:1704.08370 [astro-ph.HE].
- [43] J. D. Schnittman, *Phys. Rev. D* **70**, 124020 (2004).
- [44] J. S. Speagle, *MNRAS* **493**, 3132 (2020), <https://academic.oup.com/mnras/article-pdf/493/3/3132/32890730/staa278.pdf>.
- [45] C. Talbot, R. Smith, E. Thrane, and G. B. Poole, *Phys. Rev. D* **100**, 043030 (2019).
- [46] B. Abbott *et al.*, “GWTC-1 BBH populations data release,” In prep.
- [47] D. Wysocki, J. Lange, and R. O’Shaughnessy, *Phys. Rev. D* **100**, 043012 (2019).
- [48] J. D. Romano and N. J. Cornish, *Living Rev. Rel.* **20**, 2 (2017), arXiv:1608.06889 [gr-qc].
- [49] T. J. Loredo, in *Bayesian Inference and Maximum Entropy Methods in Science and Engineering ed R. Fischer, R. Preuss and U. V. Toussaint*, AIP Conference Series, Vol. 735 (AIP, Melville, NY, 2004) p. 195.
- [50] M. Fishbach, D. E. Holz, and W. M. Farr, *Astrophys. J. Lett.* **863**, L41 (2018).
- [51] E. Thrane and C. Talbot, *Publ. Astron. Soc. Austral.* **36**, e010 (2019), arXiv:1809.02293 [astro-ph.IM].
- [52] I. Mandel, W. M. Farr, and J. R. Gair, *MNRAS* **486**, 1086 (2019), <http://oup.prod.sis.lan/mnras/article-pdf/486/1/1086/28390969/stz896.pdf>.
- [53] S. Husa, S. Khan, M. Hannam, P. Michael, F. Ohme, X. Jiménez Forteza, and A. Bohé, *Phys. Rev. D* **93**, 044006 (2016), arXiv:1508.07250 [gr-qc].
- [54] M. Hannam, P. Schmidt, A. Bohé, L. Haegel, S. Husa, F. Ohme, G. Pratten, and M. Pürrer, *Phys. Rev. Lett.* **113**, 151101 (2014).
- [55] S. Khan, S. Husa, M. Hannam, F. Ohme, P. Michael, X. Jiménez Forteza, and A. Bohé, *Phys. Rev. D*, 044007 (2016), arXiv:1508.07253 [gr-qc].
- [56] S. Babak, A. Taracchini, and A. Buonanno, *Phys. Rev. D* **95**, 024010 (2017), arXiv:1607.05661 [gr-qc].
- [57] A. Taracchini *et al.*, *Phys. Rev. D* **89**, 061502 (2014), arXiv:1311.2544 [gr-qc].
- [58] Y. Pan, A. Buonanno, A. Taracchini, L. E. Kidder, M. H., H. P. Pfeiffer, M. A. Scheel, and B. Szilái, *Phys. Rev. D* **89**, 084006 (2014), arXiv:1307.6232 [gr-qc].
- [59] B. Abbott *et al.* (LIGO Scientific, Virgo), *Phys. Rev. Lett.* **116**, 241102 (2016), arXiv:1602.03840 [gr-qc].
- [60] C. Hoy and V. Raymond, (2020), arXiv:2006.06639 [astro-ph.IM].

## Appendix

### Parameter estimation methods

To analyze the simulated signal, we perform Bayesian parameter estimation using the standard Gaussian likelihood for gravitational-wave data [34, 48]:

$$\mathcal{L}(d_i|\theta) = \prod_j \frac{2}{\pi T S_n(f_j)} \exp \left[ -\frac{2|d_i(f_j) - h(f_j; \theta)|^2}{T S_n(f_j)} \right], \quad (4)$$

where  $T$  is the duration of the data segment being analyzed,  $S_n(f_j)$  is the noise power spectral density of the

detector,  $d_i(f_j)$  is the strain data for event  $i$ , and  $h(f_j; \theta)$  is the waveform model for the compact binary source. In order to obtain posterior samples for the parameters  $\theta$  using the likelihood in Eq. 4, we impose priors that are uniform in the component masses  $m_1$ ,  $m_2$  between  $10 M_\odot$  and  $240 M_\odot$ , with constraints on the total mass between  $70 M_\odot$  and  $240 M_\odot$  and on mass ratio  $q$  between 0.2 and 1. The luminosity distance prior is  $\propto d_L^2$  from 1–7000 Mpc.

Using the population model  $\pi(\theta|\Lambda)$  to describe the distribution of individual-event parameters  $\theta$ , the likelihood of observing the hierarchical parameters  $\Lambda$  for a data set  $\{d\}$  consisting of  $N_{\text{det}}$  detected events is given by:

$$\mathcal{L}(\{d\}|\Lambda) \propto \prod_{i=1}^{N_{\text{det}}} \frac{\int \mathcal{L}(d_i|\theta)\pi(\theta|\Lambda)}{\alpha(\Lambda)} \quad (5)$$

where  $\alpha(\Lambda)$  represents the detectable fraction of events assuming the individual-event parameters are drawn from distributions specified by hyper-parameters  $\Lambda$  [47, 49–52]. We use the sensitive spacetime volume estimates released by the LVC in [22] determined through an injection campaign [31] for  $\alpha(\Lambda)$  and evaluate the likelihood in Eq. 5 using a Monte Carlo integral over the individual-event parameter posteriors released by the LVC for the binary black hole events included in GWTC-1 [30, 31]. The posterior population distribution calculated using the hyper-parameter posteriors obtained using the likelihood in Eq. 5 is given by:

$$\text{PPD}(\theta|\{d\}) = \int \pi(\theta|\Lambda)p(\Lambda|\{d\})d\Lambda. \quad (6)$$

The Beta distribution described in Eq. 1 can also be parameterized in terms of its mean and variance:

$$\mu(\chi) = \frac{\alpha}{\alpha + \beta}, \quad (7)$$

$$\sigma^2(\chi) = \frac{\alpha\beta}{(\alpha + \beta)^2(\alpha + \beta + 1)}. \quad (8)$$

We choose to sample in  $\mu(\chi)$  and  $\sigma^2(\chi)$ , imposing constraints such that  $\alpha, \beta > 0$ . The distribution for spin tilt angles is given by the sum of an isotropic component and a preferentially aligned component, which is composed of the product of two truncated Gaussian peaked at  $\cos t_i = 1$  for each tilt angle:

$$p(\cos t_{1/A}, \cos t_{2/B}|\sigma_{1/A}, \sigma_{2/B}, \xi) = \frac{1 - \xi}{4} + \frac{2\xi}{\pi} \prod_{i \in \{1/A, 2/B\}} \frac{\exp(-(1 - \cos t_i)^2/(2\sigma_i^2))}{\sigma_i \text{erf}(\sqrt{2}/\sigma_i)}. \quad (9)$$

The hyper-parameter  $\xi$  gives the mixture fraction between the two components and is largely unconstrained—and was found in [22]—and unchanged between the inference performed on the mass-sorted and spin-sorted samples.

Parameter	Min	Max
$\alpha_m$	-0.8	3.23
$m_{\max}$	30 $M_{\odot}$	58 $M_{\odot}$
$m_{\min}$	5 $M_{\odot}$	–
$\beta_m$	0	–
$\mu(\chi)$	0	1
$\sigma^2(\chi)$	0	0.25
$\xi$	0	1
$\sigma_{1/A}$	0	4
$\sigma_{2/B}$	0	4

TABLE II. Prior ranges for the hyper-parameters used in our population analysis. The minimum primary mass,  $m_{\min}$ , was fixed to 5  $M_{\odot}$ , and the power-law index for the distribution of mass ratios,  $\beta_m$ , was fixed to 0.

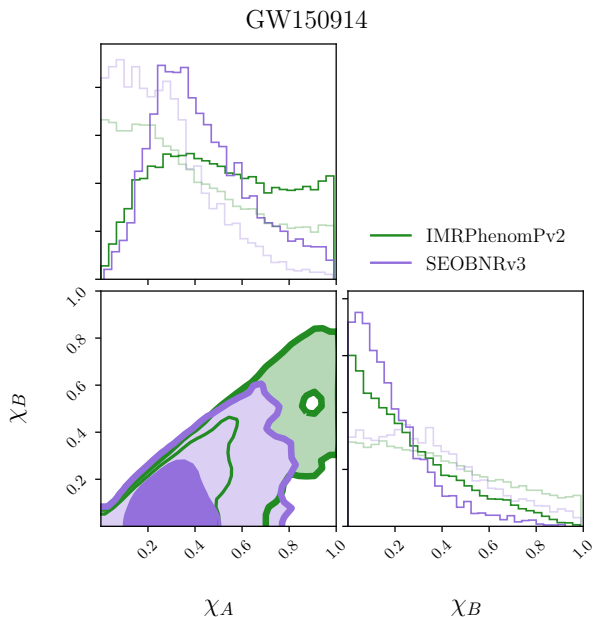


FIG. 5. Comparison corner plot for the spin magnitudes for the posteriors obtained using both the IMRPhenomPv2 (green) and SEOBNRv3 (purple) waveforms for GW150914 using the spin sorting. The marginalized posteriors obtained using the mass sorting are shown in lighter green and purple.

We use uniform priors on all hyper-parameters, the ranges of which can be found in Table II.

We obtain values for the mass hyper-parameters comparable to those quoted in [22] despite using a prior range limited by the released spacetime volume estimates:  $\alpha = 0.53^{+1.24}_{-1.13}$ ,  $m_{\max} = 41.61^{+8.46}_{-4.76} M_{\odot}$ , with uncertainties quoted at the 90% credible level.

### Additional results for individual events

For certain events, we note significant differences in the posteriors obtained with the two different waveform models applied to BBHs in GWTC-1: IMRPhenomPv2 [53–

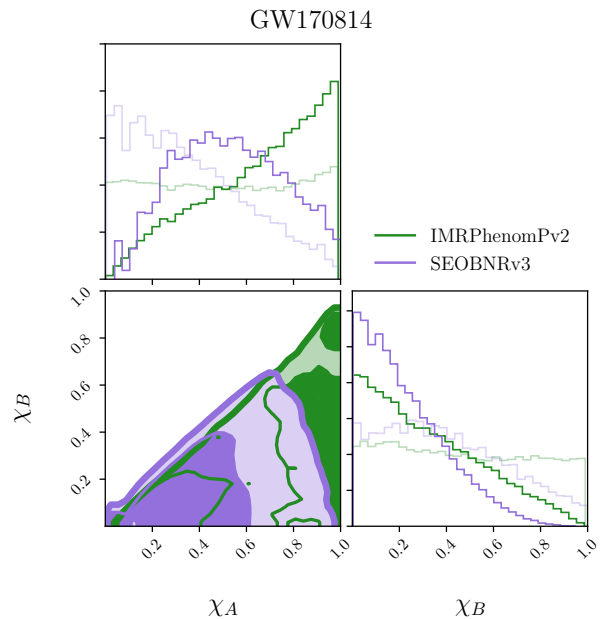


FIG. 6. Comparison corner plot for the spin magnitudes for the posteriors obtained using both the IMRPhenomPv2 (green) and SEOBNRv3 (purple) waveforms for GW170814 using the spin sorting. The marginalized posteriors obtained using the mass sorting are shown in lighter green and purple.

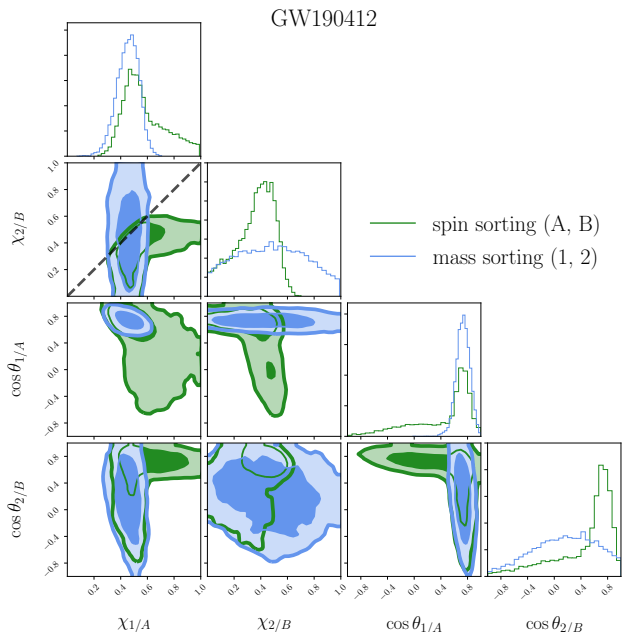


FIG. 7. Comparison corner plot for the spin magnitudes and tilts for the posteriors obtained using the SEOBNRv4PHM waveform for GW190412.

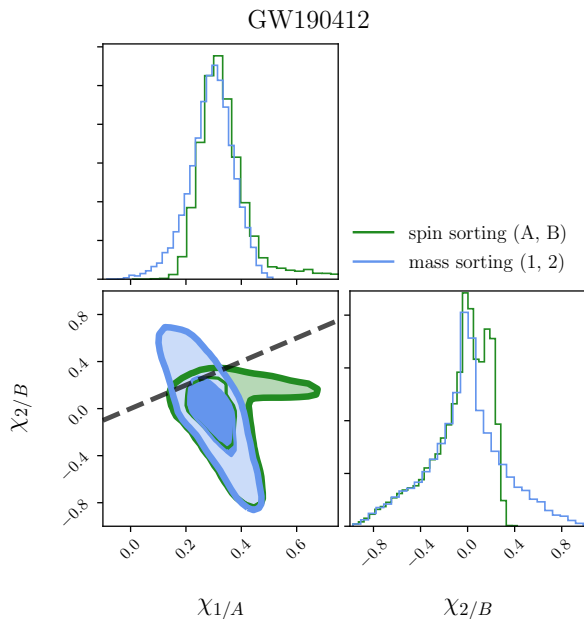


FIG. 8. Comparison corner plot for the spin magnitudes for the posteriors obtained using the aligned-spin waveform SEOBNRv4HM\_ROM for GW190412 using both the spin (green) and mass (blue) sorting. Negative values of  $\chi$  are included due to anti-alignment.

55], which uses an effective precessing spin model, and SEOBNRv3, which uses a fully precessing spin model [56–58]. For GW150914, the one-dimensional posterior for  $\chi_A$  is much more tightly constrained for SEOBNRv3, with  $\chi_A = 0.39^{+0.44}_{-0.24}$  compared to  $\chi_A = 0.49^{+0.45}_{-0.38}$  for IMRPhenomPv2, a feature which is not as easily recognizable in the  $\chi_1$  posterior. A comparison of the spin magnitudes obtained using both waveform models is shown in Fig. 5. Similarly for GW170814, the posterior for  $\chi_A$  turns over at around  $\chi_A \sim 0.5$  for SEOBNRv3, but not for IMRPhenomPv2 (Fig. 6). The two-dimensional  $\chi_A, \chi_B$  posterior recovered with SEOBNRv3 is also much more tightly clustered around low spins for both GW170814 and GW170818, although these features are distinguishable in the  $\chi_1, \chi_2$  posteriors as well.

For the unequal-mass binary GW190412 [33], the spin sorting introduces degeneracies in the spin parameters that were not present in the mass-based sorting. The

one-dimensional  $\chi_A$  posterior is much less constrained than  $\chi_1$ , and it features a tail extending to higher spin magnitudes. Unlike for the other BBH signals, which are consistent with  $q = 1$ , the tilt posteriors for this event change considerably between the mass and spin sortings. There is a clear degeneracy observed between  $\theta_A$  and  $\theta_B$  where either one or the other is constrained to lie in the orbital plane, similar to the pattern observed for  $\theta_1$  and  $\theta_2$  in our simulated signal. The  $\chi_B$  posterior is more constrained than the  $\chi_2$  posterior, peaking at  $\chi_B \sim 0.5$  and ruling out  $\chi_B \gtrsim 0.7$  with  $3\sigma$  credibility across the various waveforms allowing spin precession. Fig. 7 compares the posteriors on the spin magnitudes and tilts for both the spin and mass sorting obtained using a waveform model that allows for spin precession. Based on the application of the spin sorting to this event, we conclude that it is preferable to use the mass sorting when the mass ratio of the binary can be clearly constrained away from equal mass, as expected from our simulations.

When analyzing the posteriors obtained for GW190412 with aligned-spin waveforms, the  $\chi_1, \chi_2$  posterior shows a strong correlation depending on orientation with respect to  $\vec{L}$ : high, aligned primary spins are allowed when the secondary spin is high and anti-aligned; low, aligned primary spins are allowed when the secondary spin is high and aligned. This correlation, which is due to the strong constraint on the effective aligned spin,  $\chi_{\text{eff}}$ , is simply reflected over the  $\chi_A = \chi_B$  boundary when the posteriors are projected into the spin sorting.

### Spin disk plots

In Figs. 9–13, we show the spin disk plots for the spin-sorted posterior samples for all of the current LVC detections (see e.g. Fig. 5 of [59]) calculated using PESummary [60]. The angular direction indicates the misalignment with the orbital angular momentum, while the radial direction shows the spin magnitude for the highest-spinning compact object on the left and the least-spinning object on the right. We show the posterior samples obtained using the IMRPhenomPv2 waveform for BBH events reported in GWTC-1, IMRPhenomPv2\_NRTidal with the high-spin prior for the two BNS detections, and IMRPhenomPv3 for GW190412.

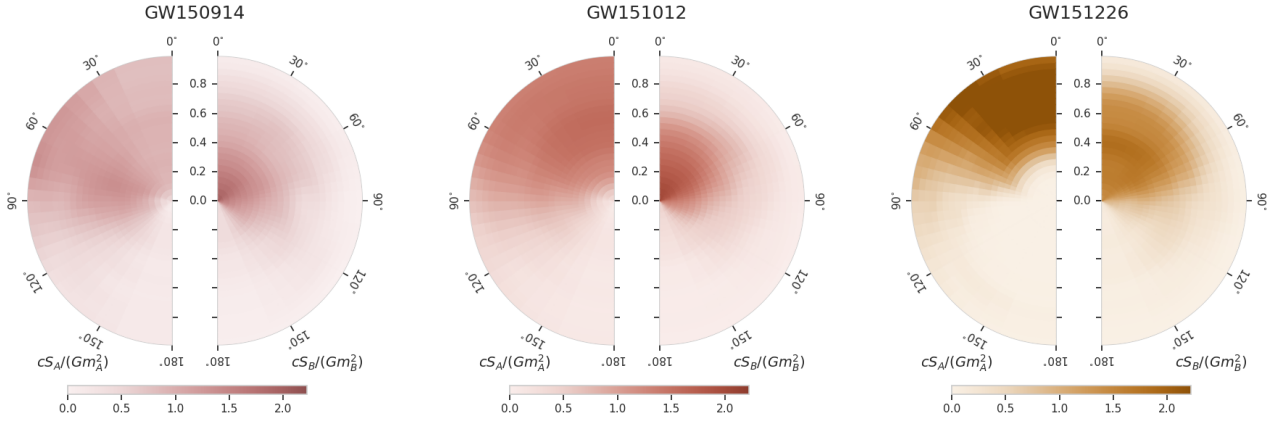


FIG. 9. Spin disk plots for the spin-sorted posterior samples for GW150914, GW151012, and GW151226

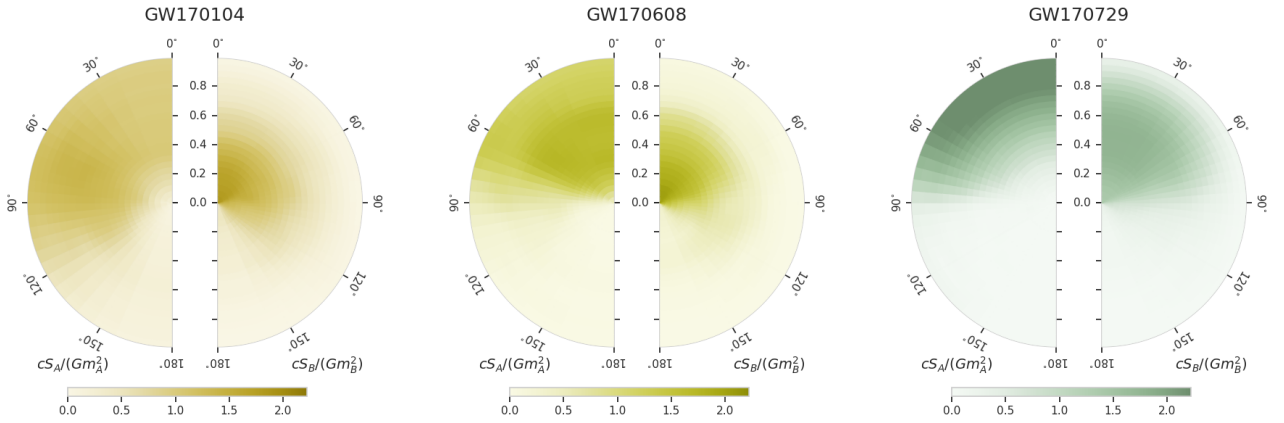


FIG. 10. Spin disk plots for the spin-sorted posterior samples for GW170104, GW170608, and GW170729

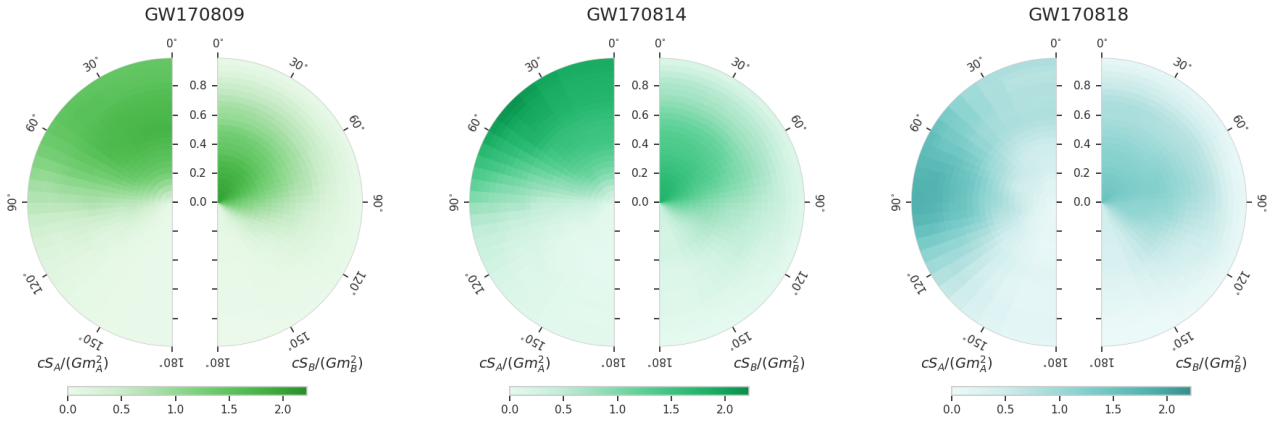


FIG. 11. Spin disk plots for the spin-sorted posterior samples for GW170809, GW170814, and GW170817

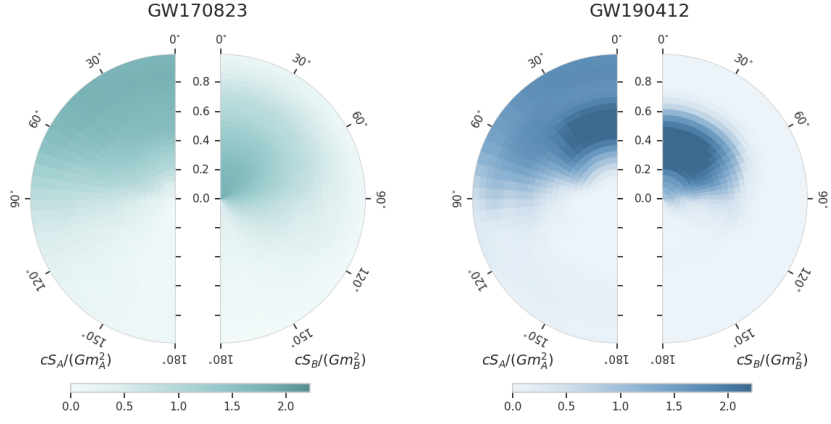


FIG. 12. Spin disk plots for the spin-sorted posterior samples for GW170823 and GW190412

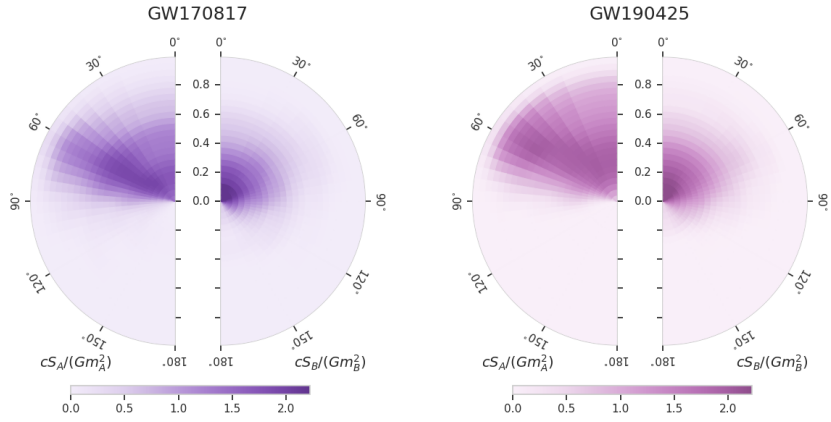


FIG. 13. Spin disk plots for the spin-sorted posterior samples for the BNS detections GW170817 and GW190425